5422 *Macromolecules* **2008**, *41*, 5422−5432

Transport Properties of Rodlike Particles

Marc L. Mansfield*,[†] **and Jack F. Douglas***,[‡]

Department of Chemistry and Chemical Biology, Stevens Institute of Technology, Hoboken, New Jersey 07030, and Polymers Division, National Institute of Standards and Technology, Gaithersburg, Maryland 20899

Received December 20, 2007; Revised Manuscript Received April 23, 2008

ABSTRACT: The transport properties of rodlike particles have been of interest since the origins of polymer science. Indeed, Staudinger initially believed that polymers had *exclusively* this structure, although Onsager soon discounted this possibility through direct computation of the transport properties of slender (ellipsoidal) particles and comparison with early polymer solution measurements. History is apparently repeating itself in the study of carbon nanotubes, which are also often assumed to be generally rodlike. Computations of the transport properties of rods have often assumed such structures could be described by ellipsoids or have relied on slender body calculations of uncertain accuracy. To clarify the situation, we apply a path-integration method to compute the intrinsic viscosity $[\eta]$ and friction coefficient f of right rectangular cylinders, cylinders with rounded ends, and other fiberlike structures having a variety of cross-sections. We then determine convenient approximants that describe these basic properties over a wide aspect ratio range and for all these cross-sectional shapes. Our computations are validated against independent boundary element computations by Aragon in the case of right rectangular cylinders. Finally, we discuss the apparent mass-scaling exponent of the intrinsic viscosity (Mark−Houwink exponent) for rodlike structures since this quantity is often reported in the polymer science literature.

1. Introduction

Recent work on the characterization of carbon nanotubes and other similar structures has generated renewed interest in the transport properties of rodlike particles.[1–12] Many of these studies have simply assumed that these structures are rodlike, ignoring observational evidence for finite persistence lengths, or other sources of flexibility. This paper is not concerned with the validity of the rodlike picture for any particular type of particle but instead with the validity of theoretical expressions of the transport properties of rods that are currently in use for the characterization of various nanoparticle structures.

Theoretical work on slender-body hydrodynamics has a long history, beginning with early contributions of Jeffery,[13] Onsager,[14] and Perrin[15] on ellipsoids of revolution. Other contributions on ellipsoids of revolution,[16–20] cylinders,[19,21–34] helices,[35,36] tori,[24,36–38] triaxial ellipsoids,[39] and many general treatments[23,40–49] have also appeared. Most theoretical results for cylinders and other nonellipsoidal shapes involve calculations whose accuracy is uncertain. We decided that it would be useful to compare the results of various approximations that have been proposed for rodlike bodies (listed in Appendix 1) against the predictions of a recently developed numerical path-integration method[50–57] that gives precise results for particles of arbitrary shape. This comparison also includes boundary-element calculations provided by Aragon,[58] which constitute an independent validation of our computations. We find that many of the expressions in active use have limited accuracy.[59] Therefore, in place of these, we provide approximants that reproduce our numerical results for both the intrinsic viscosity and the friction coefficient, where the uncertainties in the approximants are specified. These results should be helpful both in the reliable characterization of rodlike particles, and also with providing an appreciation of the inherent limitations of slender-body theory, upon which much of polymer hydrodynamics is based. Similar calculations on the wormlike chain model and on random coils will be reported in separate publications.[60,61]

Let L, d, and $r = d/2$ represent the length, diameter, and radius of any rodlike body. For any given property, we normally expect asymptotic scaling behavior in the "slender-body" limit, $L \gg d$. However, the expansion parameter of slender-body theory is $\ln(L/d)$, and asymptotic behavior is only achieved at aspect ratios around $e^{20} \approx 10^9$. Evidently, rodlike structures should exhibit the properties of semiflexible (or wormlike) polymers before they enter the true asymptotic scaling regime described by slender rods. Therefore, reliable approximations of the transport properties require an accurate determination of the corrections to the asymptotic predictions for rodlike scaling.

Our computational scheme is a numerical path integration that we have described in previous publications.[53–57] The method involves uncertainties of about 1% or less for the hydrodynamic radius, and recently has been improved to give accuracies of about 1.5% or less for the intrinsic viscosity.[62] In order to better understand the influence of end effects on slender bodies, we have examined results for two popular models of rods, cylinders and blunt-ended cylinders (Figure 1).

The hydrodynamic radius, R_h, is the proportionality constant between the friction coefficient and the solvent viscosity, $f = 6\pi\eta R_h$. Through the Einstein relation, $D = kT/f$, it is also related to the diffusivity. The intrinsic viscosity, $[\eta]$ is the leading virial coefficient for the solution viscosity when the solute concentration is measured in volume fraction units:

$$\eta = \eta_0(1 + [\eta]\phi + ...) \qquad (1)$$

where η, η_0, and ϕ are the solution viscosity, the solvent viscosity, and the volume fraction, respectively. Therefore, $[\eta]$ is a dimensionless, scale-invariant functional of the shape of the particle. The quantity that is most frequently encountered in experimental work, the "practical" intrinsic viscosity, $[\eta]_P$, is the viscosity virial coefficient when solute concentration is measured in mass/volume units. The two are related by the simple conversion:

---

* Corresponding authors. E-mail: (M.L.M.) marc.mansfield@stevens.edu; (J.F.D.) jack.douglas@nist.edu.

[†] Department of Chemistry and Chemical Biology, Stevens Institute of Technology.

[‡] National Institute of Standards and Technology.

10.1021/ma702839w CCC: \$40.75

$$[\eta]_{\mathrm{P}} = \frac{V[\eta]}{m} \tag{2}$$

for V and m the volume and mass of the particle, respectively. The product $J = V[\eta] = m[\eta]_P$ has units of volume and is a measure of the volume of the region over which Stokes flow is perturbed by the body. The quantity

$$V_{\mathrm{h}} = \frac{2J}{5} = \frac{2}{5}V[\eta] = \frac{2}{5}m[\eta]_{\mathrm{P}} \tag{3}$$

is known as the "hydrodynamic volume," and equals the volume of an equivalent sphere, since for the sphere, we have the Einstein result $[\eta] = {}^5/_2$.

We emphasize that the appropriate comparison, when replacing any complex particle with a simpler effective body, such as a helix with a cylinder or a globular molecule with a sphere, should be between the hydrodynamic volumes of the two bodies, eq 3, and not their intrinsic viscosities. The best way to see this is to rewrite eq 1 as

$$\eta = \eta_0\left(1 + [\eta]\frac{NV}{V_{\mathrm{tot}}} + ...\right) \tag{4}$$

where V_{tot} is the total volume of the solution, and N is the number of solute particles present. Replacing the actual solute particles, one for one, with some standard hypothetical particle will only have the same hydrodynamic effect if the product $J = V[\eta]$ is the same for the two particles. Therefore, a rodlike particle and its effective cylinder will have the same hydrodynamic volume, but since their actual volumes can differ substantially, then so also can their intrinsic viscosities.[63] Likewise, it is obvious from Stokes' law, $f = 6\pi\eta R_{\mathrm{h}}$, that particles that are hydrodynamically equivalent with respect to friction must have the same hydrodynamic radii.

In this paper, we use the terms "rod" or "rodlike" to represent straight, slender, nontapering structures. By this definition, both cylinders and blunt-ended cylinders are rodlike. A rigid helix is also rodlike: It has a uniformly periodic profile along its length and does not taper off toward the ends. Because of the availability of exact solutions for ellipsoids of revolution,[13–16,18] and because of the expectation of universal scaling behavior at sufficiently high aspect ratios, there has been a repeated tendency over the years to use highly prolate ellipsoids of revolution as a model of rodlike particles. Another goal of this paper is to point out the pitfalls of such an approach, which was also observed by Haltner and Zimm[19] based on direct measurements on macroscopic cylinders and ellipsoids. We will show that because ellipsoids taper toward either end, they do not have the same longitudinal Stokes force distribution as cylinders and other nontapering particles. (See also Gluckman et al.[20]) This means that there are fundamental differences between the hydrodynamic properties of slender circular cylinders and slender prolate ellipsoids. For example, there is no single prolate ellipsoid having the same length as a given rodlike particle that can simultaneously reproduce the hydrodynamic radius and the hydrodynamic volume. Of course, these discrepancies between cylinders and ellipsoids do eventually disappear in the slender-body limit, but as already mentioned, this regime corresponds to aspect ratios of no physical interest. Furthermore, since the longitudinal mass distributions of ellipsoids and cylinders are not the same, a cylinder and an ellipsoid of the same total length do not have the same radius of gyration, R_{g}. Fortunately, with the formulas published here, as well as a few others of comparable accuracy,[28,29,32,44,64,65] it is no longer necessary to model rodlike particles as ellipsoids.[66]

We also provide computations of the dimensionless ratios $R_{\mathrm{g}}/R_{\mathrm{h}}$, R_η/R_{h}, and $R_{\mathrm{g}}^3/V[\eta]$ of rods as functions of aspect ratio, $A = L/d$, where L and d are respectively the length and diameter of the rod. Each ratio combines the results of two experiments and carries scale-invariant information about the shape of the solute particle.[67] The intrinsic-viscosity-mass scaling exponent, or the so-called Mark–Houwink exponent is also examined here since it is widely considered as a measure of particle shape. Finally, because many carbon nanotube and similar systems often have a distribution of lengths and diameters, we consider the effects of polydispersity on the intrinsic viscosity.

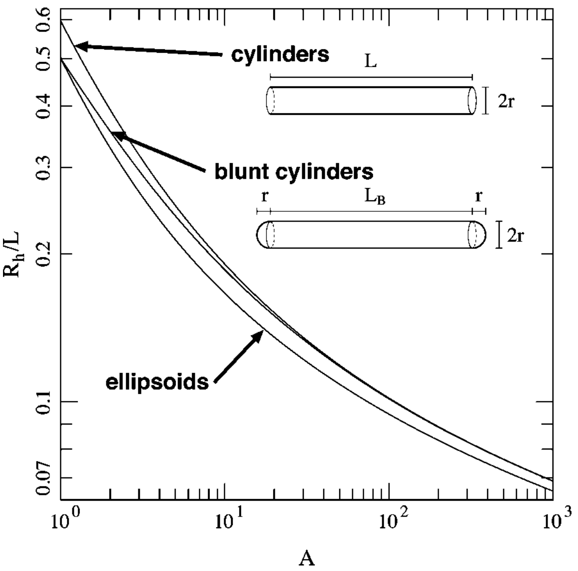

Figure 1. Ratio of hydrodynamic radius to length, R_{h}/L, for several slender bodies as a function of aspect ratio, A. Also shown are our definitions of the dimensional parameters of both cylinders and blunt cylinders.

Our computations rely on an interesting analogy between electrostatics and hydrodynamics.[50–55] For example, the charge distribution over the surface of a charged conductor is approximately proportional to the distribution of Stokes force over the same surface in Stokes flow. The following approximate proportionalities also result from the hydrodynamic–electrostatic analogy:[52]

$$R_{\mathrm{h}} = q_{\mathrm{h}}C \tag{5}$$

$$[\eta] = \frac{q_\eta\langle\alpha\rangle}{V} \tag{6}$$

where q_{h} and q_η are constants of proportionality. Here, C is the electrostatic capacity, and $\langle\alpha\rangle$ is the mean electrostatic polarizability, or one-third the trace of the polarizability tensor, of a perfect conductor having the same size and shape as the body. If the analogy were exact, the two terms q_{h} and q_η would be constant. In reality, they are weak, scale-invariant, dimensionless functionals of the particle shape. The functional q_{h} lies in the range

$$q_{\mathrm{h}} = 1.00 \pm 0.01 \tag{7}$$

for all bodies.[52] With such small variability, we usually assume that q_{h} is unity and that R_{h} and C are interchangeable. The variability of q_η is larger; for all shapes it lies in the range[52]

$$q_\eta = 0.79 \pm 0.04 \tag{8}$$

Given this analogy, in this paper we will shift between a hydrodynamic and an electrostatic description, as it suites us.

Our path-integration technique is rigorous (to within sampling error) for the capacity and polarizability tensor and can be applied to objects of any shape. We then infer the hydrodynamic radius and the intrinsic viscosity using eq 5 to eq 8. In a more recent development,[62] we use eq 5 to eq 7 along with an estimate for q_η obtained from the eigenvalues of the polarizability tensor,

Table 1. Volume and Gyration Radius of Model Rodlike Particles[a]

cylinders	blunt-ended cylinders
$\delta = d/L = A^{-1}$	$\delta = d/L_B = (A - 1)^{-1}$
$V = \pi L^3\delta^2/4$	$V = \pi L_B^3(\delta^2/4 + \delta^3/6)$
$R_g^2 = (L^2/12)[1 + 3\delta^2/2]$	$R_g^2 = (L_B^2/12)[(1 + 2\delta + 3\delta^2 + 6/5\delta^3)/(1 + 8\delta)]$

[a] These formulas are exact for the models as defined in Figure 1.

which appears to give a more accurate approximation than eq 8. This latter approach requires additional testing, but initial results suggest an uncertainty of about 1.5% for the value of q_η. Unless otherwise noted, the intrinsic viscosity results described here were obtained by the latter approach.

2. Formulas for the Volume, Gyration Radius, Hydrodynamic Radius, and Intrinsic Viscosity of Cylinders

As already mentioned, we let L, r, and $d = 2r$ represent the length, radius, and diameter of a cylinder. Similarly, we let $L = L_B + d$, r, and d represent the total length, radius, and diameter of a blunt-ended cylinder, there being length contributions of L_B and d, respectively, from the cylindrical portion and the two hemispherical caps; see Figure 1. The volumes and gyration radii of either cylinder model are given in Table 1. The aspect ratios of both types of cylinders are defined as the length-to-diameter ratio:

$$A = \frac{L}{d} = \frac{L}{2r} \quad \text{(cylinder)} \tag{9}$$

$$A = \frac{L}{d} = \frac{L_B + d}{d} \quad \text{(blunt cylinder)} \tag{10}$$

The hydrodynamic radius and intrinsic viscosity of both models obey the following asymptotic forms as $A \rightarrow \infty$:[25,47]

$$\frac{R_h}{r} \rightarrow \frac{A}{\ln A} \quad \text{(cylinder)} \tag{11}$$

$$[\eta] \rightarrow \frac{8A^2}{45 \ln A} \quad \text{(cylinder)} \tag{12}$$

The analogous expressions for ellipsoids of revolution (major axis = c, minor axis = a, $A = c/a$) are as follows:[14,47]

$$\frac{R_h}{a} \rightarrow \frac{A}{\ln A} \quad \text{(prolate ellipsoid)} \tag{13}$$

$$[\eta] \rightarrow \frac{4A^2}{15 \ln A} \quad \text{(prolate ellipsoid)} \tag{14}$$

Convergence to these asymptotes occurs only when $\ln A \gg 1$, and eqs 11–14 are in significant error anywhere within the range of physically realizable aspect ratios. For example, we find that eqs 11 and 12 are in error by about 2% and 4%, respectively, even at $A = 10^9$. Appendix 1 summarizes a few formulas from the literature that have been presented in attempts to improve on these asymptotic expressions. In this section, we present our own results as alternatives to the formulas in Appendix 1.

As already mentioned, we computed the hydrodynamic radius and the intrinsic viscosity of cylinders and ellipsoids of revolution as a function of aspect ratio by our path-integral formalism, with results displayed in Figures 1 and 2. Because the logarithmic scales of these plots deemphasize the relative errors, we point out that the discrepancies in Figure 1 vary from 19% at $A = 1$ to 5% at $A = 10^3$. Similarly, in Figure 2 they vary from 13% to 34%. The resulting data were used to develop several Padé approximants. One set of these, which we will refer to as the "higher-accuracy" approximants, are extremely accurate (typically four significant figures). However they are also quite cumbersome, and therefore are given in the supporting material accompanying this article.[68] Below, we give several "lower-accuracy" approximants for the hydrodynamic radius and intrinsic viscosity. These are more succinct but still reproduce the raw integration data to better than about 0.5%. In the following, we have

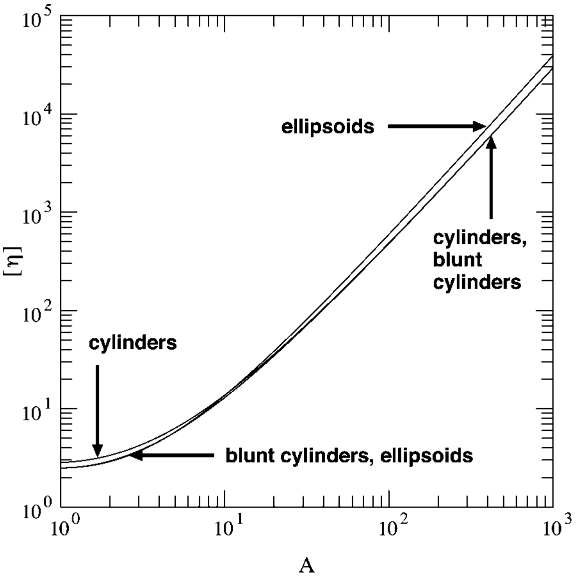

Figure 2. Intrinsic viscosity of several slender bodies as a function of aspect ratio.

$$t = (\ln A)^{-1} \tag{15}$$

for the expansion parameter of slender-body theory.

Hydrodynamic Radius. The following formula agrees with the path integration results to about 0.4% or better for cylinders in the range $0 < t < 2$ or $1.65 < A < \infty$:

$$\frac{R_h}{r} = A\left[\ln\left(\frac{4A}{e}\right)\right]^{-1} \times \left[\frac{1 - 0.782t + 0.691t^{1.67} + 0.622t^{1.77} + 0.418t^{2.16}}{1 - 0.677t + 1.601t^{2.07} + 0.178t^{2.26}}\right] \quad (\text{cylinders}, 1.65 < A < \infty) \tag{16}$$

The analogous formula for blunt cylinders, valid to better than about 0.5% in the range $0 < t < 2$ or $1.65 < A < \infty$, is as follows:

$$\frac{R_h}{r} = A\left[\ln\left(\frac{4A}{e}\right)\right]^{-1} \times \left[\frac{1 - 0.755t + 0.648t^{1.57} + 0.581t^{1.7} + 0.405t^{2.06}}{1 - 0.647t + 1.612t^{1.98} + 0.231t^{2.3}}\right] \quad (\text{blunt cylinders}, 1.65 < A < \infty) \tag{17}$$

Over the narrower range $0 < t < 0.45$ or $9 < A < \infty$, the following formula, applicable to blunt cylinders, exceeds the accuracy of eq 17, being accurate to better than 0.06%:

$$\frac{R_h}{r} = A[\ln A + \ln 4 - 1 - 3.95t^2 + 16.18t^3 - 16t^4]^{-1} \quad (\text{blunt cylinders}, 9 < A < \infty) \tag{18}$$

Each of the above expressions corresponds to the Miles formula[64] (see also section 3 and Appendix 1) with correction terms.

Intrinsic Viscosity. The following two formulas apply to cylinders and blunt cylinders, respectively, in the ranges $0 < t < 1$ or $2.72 < A < \infty$. They are Yamakawa's formula,[25] (see

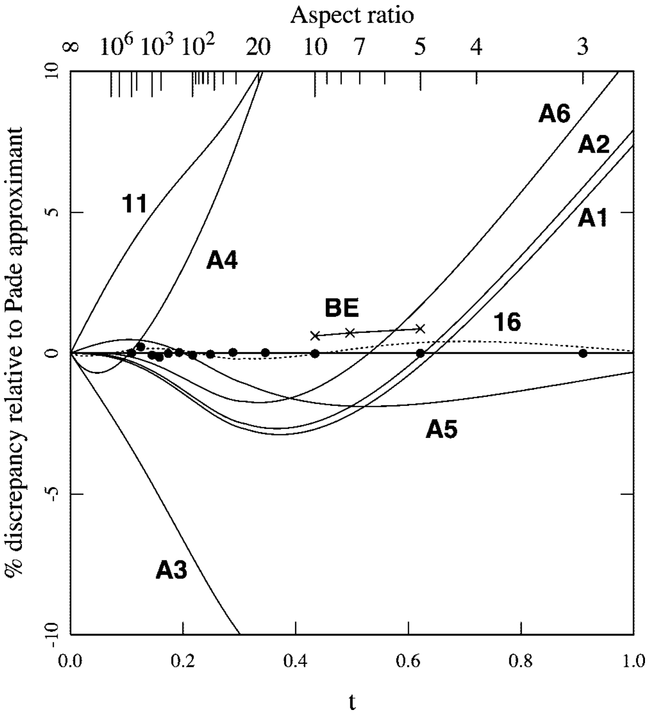

Figure 3. Comparison of various computations of the hydrodynamic radius of cylinders. The percent discrepancy relative to the more accurate Padé approximant is plotted here as a function of $t = 1/(\ln A)$, for A the aspect ratio. The aspect ratio itself is shown along the upper scale. Filled circles are the results of path integrations. The crosses, labeled BE, are the results of boundary element computations.[58] The dashed curve labeled 16 results from the less accurate Padé approximant, eq 16. All other curves are labeled with the number of the equation with which they were generated.

also Appendix 1) but each with its own correction term. They reproduce the raw integration data to 0.5% and 0.4% or better, respectively.

$$[\eta] = \frac{8A^2}{45}\left[\ln\left(\frac{4A}{e^{25/12}}\right)\right]^{-1} \times \left[\frac{1 - 1.178t + 1.233t^{1.86} + 1.925t^{6.28} + 0.652t^{12.67}}{1 - 1.094t + 0.757t^{3.76} + 1.344t^{3.83} + 1.978t^{12.07}}\right] \quad \text{(cylinders, } 2.72 < A < \infty) \quad (19)$$

$$[\eta] = \frac{8A^2}{45}\left[\ln\left(\frac{4A}{e^{25/12}}\right)\right]^{-1} \times \left[\frac{1 - 0.824t + 1.024t^{1.86} - 0.082t^{4.22} + 1.331t^{6.36}}{1 - 0.773t + 1.202t^{3.77} + 0.527t^{3.85} + 1.088t^{10.65}}\right] \quad \text{(blunt cylinders, } 2.72 < A < \infty) \quad (20)$$

The following formula is obtained from a Padé variable that is very accurate for the polarizability of blunt cylinders; its main source of uncertainty arises from the use of eq 8 for q_η. It represents the intrinsic viscosity of blunt cylinders to 4% or better at all aspect ratios above 7.

$$[\eta] = \frac{1.58A^3}{3(3A-1)}\left[\ln\left(\frac{4A}{e^{7/3}}\right) - t^{1.72}(4.53 - 18.3t + 18t^2)\right]^{-1} \quad \text{(blunt cylinders, } 7 < A < \infty) \quad (21)$$

Figures 3–6 plot the percent error in a number of different computations of the hydrodynamic radius and the intrinsic viscosity using the higher-accuracy Padé approximants as standards. These include the lower-accuracy approximants, eq 16–21; the formulas given in Appendix 1; the results of boundary element calculations performed by Aragon;[58] and the results of numerical path integrations. Figures 3–6 are plotted

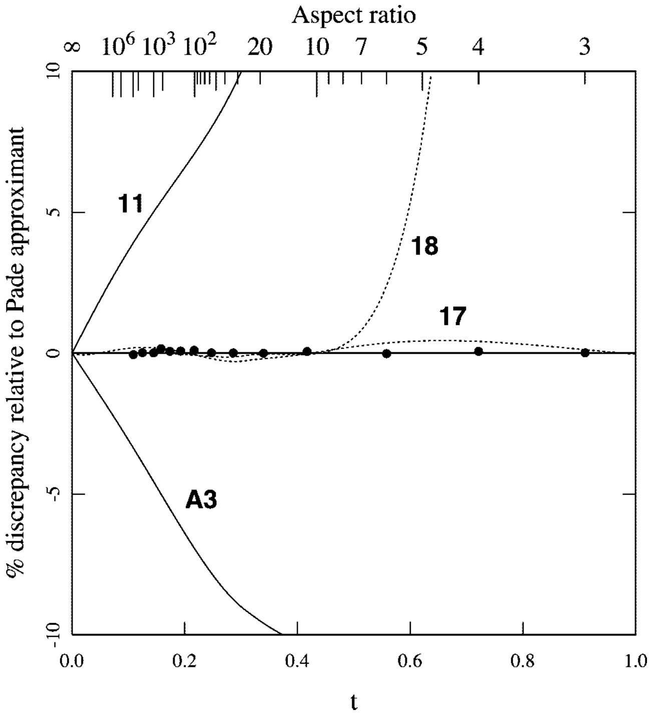

Figure 4. Comparison of various computations of the hydrodynamic radius of blunt cylinders. The percent discrepancy relative to the more accurate Padé approximant is plotted as a function of $t = 1/\ln A$. Filled circles are the results of path integrations. Dashed curves result from the two Padé approximants, eqs 17 and 18. The other two curves result from eqs 11 and A3.

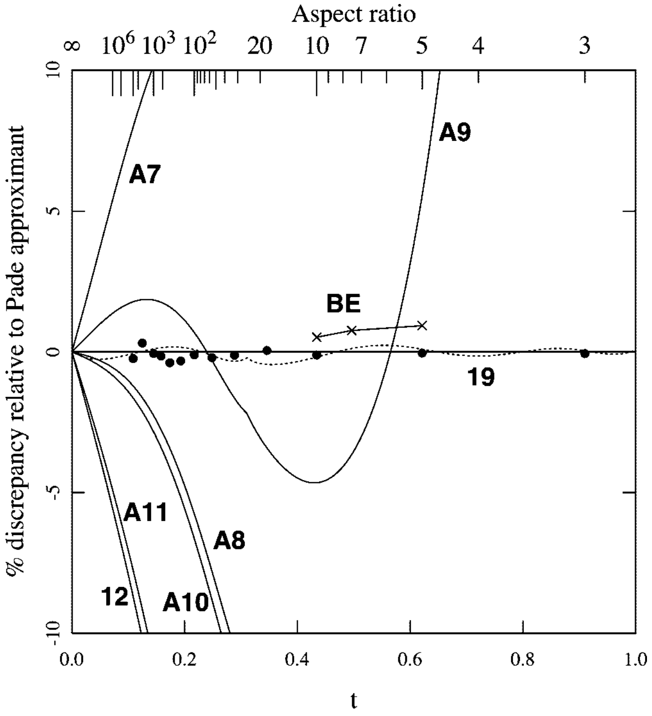

Figure 5. Comparison of various computations of the intrinsic viscosity of cylinders. The percent discrepancy relative to the more accurate Padé approximant is plotted as a function of $t = 1/(\ln A)$. Filled circles are the results of path integrations. The crosses, labeled BE, are the results of boundary element computations. [58] The dashed curve is computed from the less accurate Padé approximant, eq 19. All other curves are labeled with the number of the equation with which they were generated.

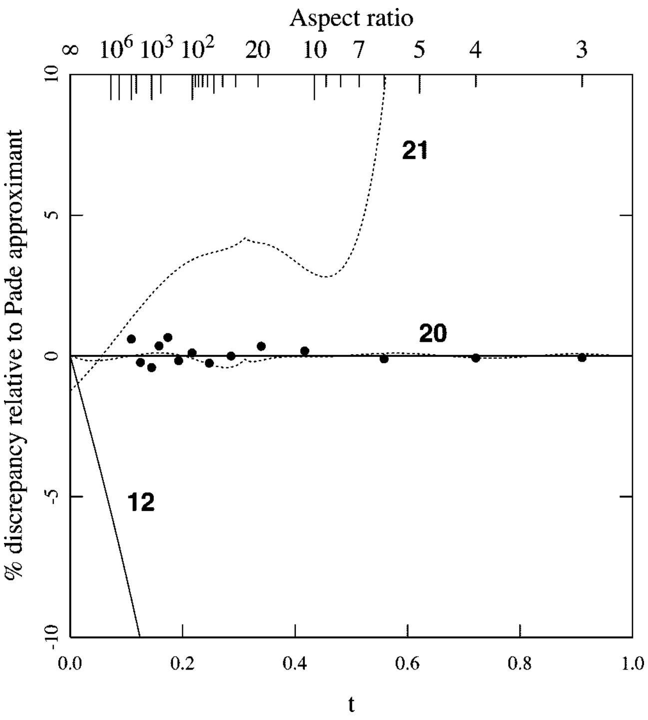

Figure 6. Comparison of various calculations of the intrinsic viscosity of blunt cylinders. The percent discrepancy relative to the more accurate Padé approximant is plotted as a function of $t = 1/\ln A$. Filled circles are the results of path integrations. Dashed curves result from the two Padé approximants, eq 20 or 21. The result due to eq 12 is also plotted.

linearly in $t = (\ln A)^{-1}$ to emphasize that all the formulas eventually converge to the asymptotes, eqs 11 or 12, as $A \rightarrow \infty$, but only as rapidly as ln A. We see that at physically realistic aspect ratios, Figures 3–6 display significant variations between the different formulas. (The uncertainty implied by these disparate results was an initial motivation of the present work.) The most successful of the formulas from Appendix 1 are the Tirado-de la Torre,[28,29,32,65] Batchelor,[44] and Miles[64] formulas, eqs A2, A5, and A6, respectively, for the hydrodynamic radius; and the Miles formula, eq A9, for the intrinsic viscosity. The Miles formalism is discussed more fully in the following section. Figure 3–6 also demonstrate that predictions based either on the asymptotes, eqs 11 or 12, or on the ellipsoid with the same length and aspect ratio, eqs A3 and A11, are not particularly accurate.

An experimental test of these formulas is provided by the tobacco mosaic virus (TMV). Treating the virus as a cylinder with $d = 18$ nm, $L = 300$ nm, and $M = 3.9 \times 10^7$daltons, the above formulas yield $R_h = 48$ nm and $[\eta]_P = 32$ cm^3/g. Experimental values for these parameters are $R_h = 49$ nm by sedimentation,[69] and $[\eta]_P = 27$ cm^3/g or 37 cm^3/g, from two different sources.[69–71]

A figure appearing in the Supporting Information shows that the differences between ordinary cylinders and blunt cylinders are of the same order of smallness as the reciprocal aspect ratio, and are therefore typical of end-effects generally. This is true in spite of the fact that the charge distribution at the sharp edge of the cylinder has a singularity, while the charge distribution on the blunt cylinder is everywhere nonsingular. The singularity is not strong enough to produce behavior qualitatively different from that of the blunt cylinder. The best way to see this is to recognize that the capacity of an ordinary cylinder is bounded below and above, respectively, by the capacities of the smallest blunt cylinder that completely contains, and the largest blunt cylinder that is completely contained by, the cylinder.

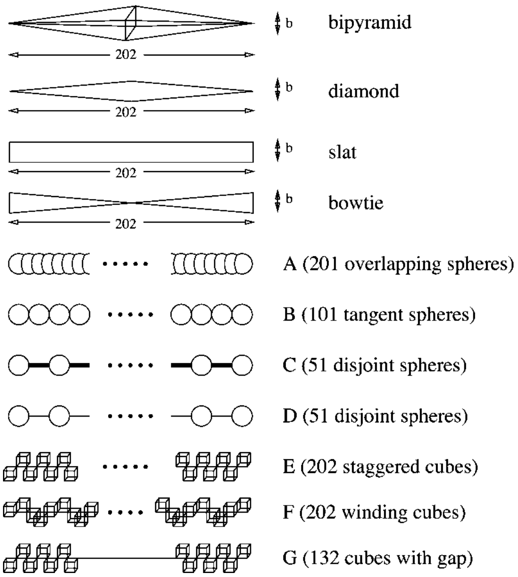

Figure 7. Schematic diagrams of slender-body models.

3. Hydrodynamically Equivalent Cylinders of General Rodlike Particles

Typical rodlike particles, e.g., helices, lack the complete symmetry of a cylinder. Nevertheless, it seems reasonable to use cylinders to model such objects. On the other hand, because they do not taper toward the ends, the practice of representing such particles with ellipsoids is more questionable. Here we show that we can replace a rodlike particle such as a helix with an equivalent hydrodynamic cylinder which has the same length and which simultaneously reproduces the hydrodynamic radius, the hydrodynamic volume, and the radius of gyration. We will also show below that there is no single corresponding equivalent ellipsoid. Specifically, two different ellipsoids are needed to match the hydrodynamic radius and the hydrodynamic volume of a nontapered rod, and neither of these reproduces the radius of gyration. We are forced to conclude that the notion of an equivalent ellipsoid is ill-founded.

Figure 7 displays several model chains considered in this section. Some are helical, some have uniform cross-sections, while some taper either toward the ends or the center. We use the term "bi-pyramid" to represent two highly elongated pyramids with square bases joined at their bases. "Diamonds", "slats", and "bowties" are two-dimensional elongated objects. The models labeled A through D are chains of spheres: Model A consists of 201 overlapping spheres, each of radius 1 and centered at the points ±100, ±99, ±98,..., 0. Model B consists of 101 spheres, also of radius 1 and centered at the points ±100, ±98, ±96,..., 0. Models C and D both consist of 51 spheres, again of radius 1 and centered at ±100, ±96, ±92,..., 0. Models C and D differ in that model C also contains a slender rod of diameter 0.2 running down the axis, while in model D the central rod has diameter 0. Models E through G are constructed from unit cubes. Model E has 202 cubes staggered between opposite quadrants of the $x-y$ plane, while model F has 202 cubes rotating through the four quadrants, generating a helix. Model G was constructed by beginning with model E and then removing 70 central cubes. The path-integration method has also been applied to determine the transport properties of these chains.

In addition to the problem of finding a single ellipsoid which models any given cylinder, we also find that the longitudinal Stokes force distribution along an ellipsoid is significantly different from that of a cylinder. Therefore, we can also expect other aspects of the respective dynamics to be fundamentally

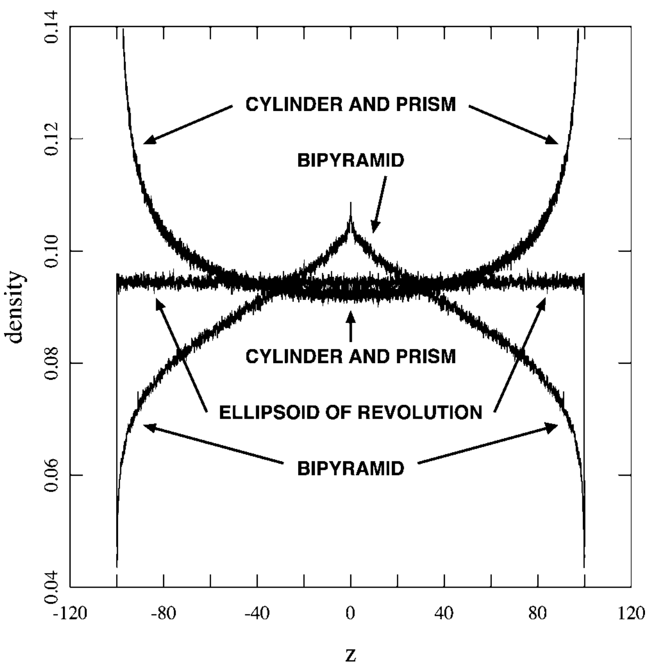

Figure 8. Longitudinal charge distribution on several slender bodies. Cylinders and prisms have indistinguishable distributions that are maximized at the ends, the distribution along bypiramids is maximum at the middle. Ellipsoids of revolution have uniform longitudinal distributions.

different. This behavior is obvious in Figure 8, which compares the longitudinal charge densities along a cylinder, an ellipsoid, a bipyramid, all of aspect ratio 100, and a rectangular prism of aspect ratio 117.6, so chosen because it possesses approximately the same capacity and polarizability as the cylinder. All four bodies have the same dimensionless length, 200. At the resolution of our calculation, the cylinder and the prism have identical longitudinal charge densities. Also note that the ellipsoid has a uniform charge density, as expected.[72] By the hydrodynamic−electrostatic analogy, this calculation indicates that the stress distribution on tapered bodies in Stokes flow is fundamentally different from that on bodies with uniform cross-sections, such as the prism or the cylinder. (See also Gluckman et al.[20]) Therefore, we can expect a level of dynamical similarity between the cylinder and the prism which cannot be expected for ellipsoids or other tapering bodies.

As already mentioned, we define an effective cylinder to be the cylinder that has the same length, the same hydrodynamic radius, and the same hydrodynamic volume as some rodlike particle. Within the electrostatic-hydrodynamic analogy, the analogous properties are the length; the capacity, C, since $R_{\mathrm{h}} = q_{\mathrm{h}}C$; and the longitudinal polarizability, $\alpha_{||}$, since $V_h = (2q_\eta/5)\langle\alpha\rangle = (2q_\eta/15)(\alpha_{||} + 2\alpha_\perp) \approx (2q_\eta/15)\alpha_{||}$. (The last approximation holds because the longitudinal polarizability component for slender bodies, $\alpha_{||}$, is much larger than the transverse component, $\alpha_\perp$.) Therefore, our definition of an effective cylinder corresponds to a cylinder having the same total length, the same electrostatic capacity, and the same longitudinal polarizability as the given slender body. By the electrostatic−hydrodynamic analogy, such a cylinder will also be an effectively equivalent hydrodynamic cylinder.

Miles has developed a formalism, based on prolate-spheroidal harmonics, to treat the electrostatic properties of slender bodies.[64] The predictions of the formalism for R_h and $[\eta]$of cylinders are given in Appendix 1. The formalism is also very instructive concerning the problem of determining an effective hydrodynamic cylinder for any arbitrary slender body. A slender body of total length L is assumed to lie along the z-axis between the points $z = \pm L/2$. In cylindrical−polar coordinates (r, z, ϕ), we can specify the surface of the body by giving r as some function of z and ϕ. We also introduce the reduced coordinate $\xi = 2z/L$. Therefore, the surface of the slender body is given by some function $r(\xi, \phi)$, defined on the intervals $\xi \in [-1, 1]$ and $\phi \in [0, 2\pi]$. We define two different mean radii, $\bar{r}$ and $\hat{r}$, as follows:

$$\ln \bar{r} = \frac{1}{4\pi}\int_0^{2\pi} \mathrm{d}\phi \int_{-1}^{+1} \mathrm{d}\xi \ln r(\xi, \phi) \tag{22}$$

$$\ln \hat{r} = \frac{1}{4\pi}\int_0^{2\pi} \mathrm{d}\phi \int_{-1}^{1} \mathrm{d}\xi\, 3\xi^2 \ln r(\xi, \phi) \tag{23}$$

According to these definitions, $\bar{r}$ and $\hat{r}$ are respectively the geometric means of $r(\xi,\phi)$ and $r(\xi,\phi)^{3\xi^2}$. Then, according to Miles, we have

$$C = \frac{L}{2}\left[\ln\left(\frac{L}{2\bar{r}}\right) + \ln 4 - 1 + O\left(\frac{\bar{r}}{L}\right)\right]^{-1} \tag{24}$$

and

$$\alpha_{||} = \frac{\pi L^3}{6}\left[\ln\left(\frac{L}{2\hat{r}}\right) + \ln 4 - \frac{7}{3} + O\left(\frac{\bar{r}}{L}\right)\right]^{-1} \tag{25}$$

i.e., $\bar{r}$ and $\hat{r}$ are relevant, respectively, to the capacity and the polarizability.

Note that for cylinders, $r(\xi,\phi) = r$ is a constant, and we obtain trivially that $\bar{r} = \hat{r} = r$. For blunt cylinders, $r(\xi,\phi) = r$ except for small contributions at the ends, so neglecting terms of order $1/A$, we again have $\bar{r} = \hat{r} = r$. Another class of bodies are those for which $r(\xi,\phi)$ depends on ϕ but not on ξ. These have longitudinal symmetry but lack rotational symmetry and include, for example, right rectangular prisms. It is again trivial to verify that such bodies satisfy $\bar{r} = \hat{r}$. For example, right rectangular prisms of dimensions $a \times b \times b$, with $a \gg b$ satisfy $\bar{r} = \hat{r} = (0.558)b$, a result obtained by numerical integration. Another class of objects are those for which $r(\xi,\phi)$ is periodic in both ϕ and ξ. These would include, for example, bodies with helical symmetry. Again it is trivial to show that $\bar{r} = \hat{r}$ as long as the body is long enough to contain many periods.

On the other hand, bodies which taper violate $\bar{r} = \hat{r}$. For example, for ellipsoids of revolution with semimajor and semiminor axes of c and a, respectively, and with $c \gg a$, we have $\bar{r} = 2ae^{-1} \cong (0.736)a$ and $\hat{r} = 2ae^{-4/3} \cong (0.527)a$.

Figure 9 confirms the Miles predictions for cylinders, ellipsoids, and prisms. It plots two quantities, Y_C and Y_α, defined by the following equations, as functions of $t = 1/\ln A$.

$$Y_C = \frac{L}{2C \ln A} \tag{26}$$

$$Y_\alpha = \frac{\pi L^3}{6\alpha_{||} \ln A} \tag{27}$$

According to eqs 24 and 25

$$Y_C = 1 + K_C t \quad \text{with } K_C = \ln\left(\frac{2L}{\bar{r}Ae}\right) \tag{28}$$

and

$$Y_\alpha = 1 + K_\alpha t \quad \text{with } K_\alpha = \ln\left(\frac{2L}{\hat{r}Ae^{7/3}}\right) \tag{29}$$

Since K_C and K_α involve the ratio L/A, they are independent of the aspect ratio. Therefore, Miles predicts that plots of Y_C or Y_α as functions of $t = (\ln A)^{-1}$ are linear with intercepts of 1 and with slopes determined ultimately by the integrals eqs 22 and 23. Figure 9 displays such plots. As usual, we are unable to display integration data for very small t, but the expected linear behavior is still observed, with the expected intercepts and slopes. Higher-order corrections determined by curve fitting

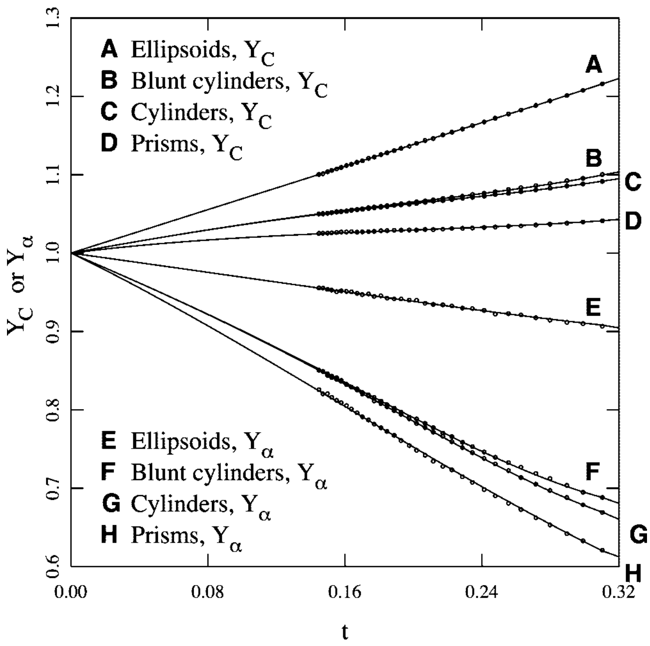

Figure 9. The Miles formalism[64] successfully predicts the approach to the infinite-length limit for cylinders, ellipsoids, and prisms. The functions Y_C and Y_α are defined in eqs 26 and 27, respectively. Circles are the results of path integrations. The solid curves are drawn according to formulas given in the supporting material, and in every case have the initial slope and intercept predicted by Miles.

are present in each of the curves of Figure 9, but the low order terms were obtained directly from the formalism, not by curve fitting. Those higher-order corrections are given in the supporting material accompanying this article.

Obviously, Miles predicts that any body which satisfies $\bar{r} = \hat{r}$ has the same capacity and the same longitudinal polarizability as a cylinder of radius $\bar{r} = \hat{r}$. However, since tapering bodies, such as ellipsoids, exhibit $\bar{r} \neq \hat{r}$, it follows that no single cylinder can simultaneously reproduce the capacity and the polarizability of a tapering body. The values of $\bar{r}$ and $\hat{r}$ eventually become irrelevant to eq 24 and eq 25, when $\ln(L/\bar{r}) \gg 1$ or when $\ln(L/\hat{r}) \gg 1$, but as already pointed out, this occurs outside the realm of physically realistic aspect ratios. Only for astronomically large aspect ratios can we say that ellipsoids and cylinders are hydrodynamically equivalent.

Given an arbitrary slender body, the Miles approach seems to hold out the possibility of determining the radius of its effective cylinder without the need of doing the path-integration. However, we find that the approach looses accuracy if the $r(\xi,\phi)$ function is too nonuniform. In fact, for some of the bodies shown in Figure 7, eqs 22 and 23 are singular. Employing a graphical construction given in the Supporting Information, we are able to determine the radius of the effective cylinder representing each of the bodies shown in Figure 7. This construction verifies that a single equivalent cylinder can always be selected to represent both the hydrodynamic volume and the hydrodynamic radius of a nontapering rodlike body. On the other hand, if the body tapers, then the cylinder reproducing the hydrodynamic volume does not simultaneously reproduce the hydrodynamic radius, and vice versa. Table 2 reports the effective cylindrical radius of each of the bodies shown in Figure 7.

Unlike hydrodynamic properties, the radius of gyration of highly prolate cylinders is insensitive to the diameter. However, tapered and nontapered slender bodies have different gyration radii. For nontapered objects, we have $R_g = L/\sqrt{12}$, for ellipsoids of revolution $R_g = L/\sqrt{20}$. For all of the rodlike bodies of Figure 7 or Table 2 that do not taper, the gyration radii are practically constant at $101/\sqrt{3} \cong 58.3$.

Table 2. Radius of the Equivalent Hydrodynamic Cylinder of Each of the Models Shown in Figure 7[a]

bipyramid	no equivalent cylinder
diamond	no equivalent cylinder
slat, $b = 1$	$r = 0.24$
slat, $b = 2$	$r = 0.50$
bowtie	no equivalent cylinder
model A	$r = 0.95$
model B	$r = 0.89$
model C	$r = 0.65$
model D	$r = 0.63$
model E	$r = 0.89$
model F	$r = 0.83$
model G	no equivalent cylinder

[a] Only nontapering rods possess an equivalent hydrodynamic cylinder, defined as having the same length, hydrodynamic radius, hydrodynamic volume, and radius of gyration.

Therefore, the appropriate equivalent model for a uniform or a periodic rodlike structure such as a helix or a carbon nanotube is *not* an ellipsoid. Ellipsoids cannot reproduce the stress distribution over the length of the body in Stokes flow. Furthermore, because of the nonuniform distribution of scattering centers along the length of the body, they cannot reproduce the radius of gyration. Rather, the appropriate equivalent model is a cylinder with the same length as the rod and with a radius adjusted to match the hydrodynamic radius and the hydrodynamic volume. We have seen that the same cylinder radius can match both simultaneously. The use of ellipsoids as equivalent models no doubt arises from the availability of closed-form expressions,[13–16,18] but as we have shown, this practice is problematic.

The Miles formalism predicts $\bar{r} = \hat{r}$ for the radius of the effective cylinder, but this is only accurate when the $r(\xi,\phi)$ function is not too nonuniform. We are unaware of any technique, aside from actually performing the path integrals, for determining the effective radius.

4. Dimensionless Ratios and the Apparent Mark−Houwink Exponent

A useful strategy in molecular characterization is to combine results of two or more experiments into dimensionless ratios, which usually are scale-invariant signatures of the shape of the particle.[67] In this section, we present results for several such ratios for cylinders. We also include an analysis of the Mark−Houwink behavior of cylinders, since the Mark−Houwink exponent is also a scale-invariant signature of particle shape.

Combining eq A2 with the expression $R_g = L/\sqrt{12}$ gives the approximation

$$\frac{R_g}{R_h} \cong 3^{-1/2}\ln(4e^{-1}A) \cong 0.223 + 1.329\log_{10}A \qquad (30)$$

leading to the prediction that R_g/R_h is linear in $\log A$. Figure 10 displays R_g/R_h calculated for both cylinders and blunt cylinders by the Padé approximant, as well as the line predicted by eq 30. All these curves are practically superimposible, verifying that linearity holds well for all aspect ratios between 10 and 10^4. (For reference, recall that the value of this ratio for a sphere is $\sqrt{0.6} = 0.775$.) The fact that the result for cylinders is indistinguishable from that for blunt cylinders indicates that the end-configuration affects both R_g and R_h in approximately the same way.

Equation 3 introduces the concept of an equivalent sphere for the intrinsic viscosity and leads to the definition of the hydrodynamic volume. We let R_η, the "viscosity radius," represent the radius of the equivalent sphere, so that

$$R_\eta = \left(\frac{3V[\eta]}{10\pi}\right)^{1/3} \qquad (31)$$

The ratio R_η/R_h also characterizes the shape.[73] Furthermore, it

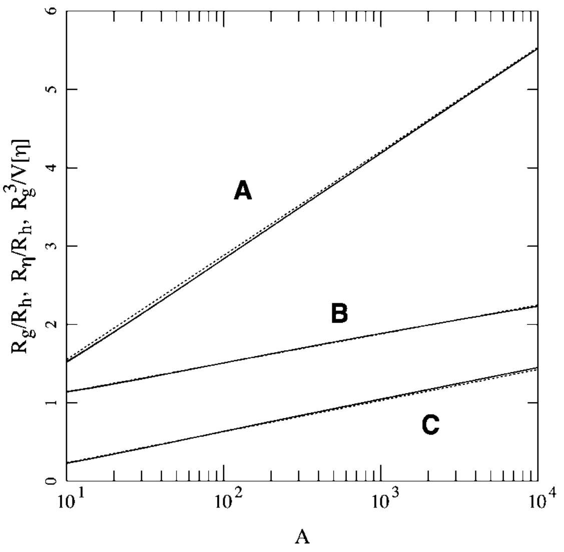

Figure 10. Dimensionless ratios R_g/R_h (A); R_η/R_h (B); and $R_g^3/V[\eta]$ (C). Curves for both ordinary and blunt cylinders are displayed as solid lines, but are unresolvable in this image. Dashed lines are linear approximations.

is related directly to the Scheraga—Mandelkern parameter

$$\beta = \frac{1}{6\pi R_h}\left(\frac{V[\eta]}{100}\right)^{1/3} \tag{32}$$

Figure 10 shows that the plot of R_η/R_h for cylinders is also indistinguishable from that for blunt cylinders. We observe that this ratio is also approximately linear in log A. The best-fit least-squares line is

$$\frac{R_\eta}{R_h} \cong 0.768 + 0.370\log_{10} A \tag{33}$$

Another ratio, $R_g^3/V[\eta]$, combines the results of viscosity and scattering measurements. This quantity is inversely proportional to the Flory—Fox parameter:

$$\Phi = \frac{V[\eta]N_A}{(6^{1/2}R_g)^3} \tag{34}$$

where N_A is Avogadro's number. In this case, eq A9 and $R_g = L/\sqrt{12}$together give the following approximation:

$$\frac{R_g^{\ 3}}{V[\eta]} \cong \frac{15}{16\pi\sqrt{3}}\ln(4e^{-7/3}A) \cong -0.163 + 0.397\log_{10} A \tag{35}$$

Figure 10 also displays the predictions of the Padé approximants for this ratio.

The agreement between eqs 30 and 35 and the more accurate calculations is attributable primarily to the fact that the Miles formulas, eqs A2 and A9, are never off by more than about 5% for aspect ratios above 10, see Figure 3 and Figure 5. A secondary reason is that some errors partially compensate when the ratios are formed. The good agreement observed for Eq. 33 is unanticipated because the expression formed from eq A2 and eq A9 (not shown here) does not imply linearity. However, its first derivative varies by only ± 9% over the entire range, so that its curvature is not noticeable. As mentioned, eq 33 is a least-squares fit.

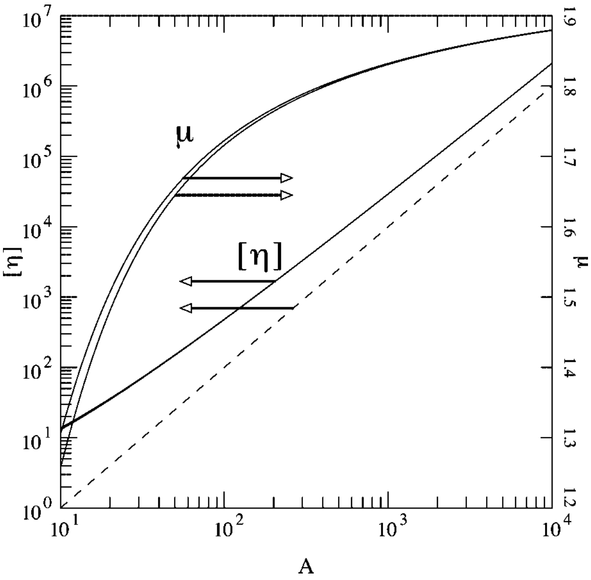

Figure 11. Mark—Houwink data for ordinary and blunt cylinders over a range of aspect ratios between 10 and 10^4. Solid curves are shown to display $[\eta]$ for both ordinary and blunt cylinders, but these are unresolvable in this image. A dashed line of slope 2 appears for reference. The Mark—Houwink exponent, μ, or the instantaneous slope of the $[\eta]$-curves, is also displayed, on a linear scale, for both blunt and ordinary cylinders, with the curve for blunt cylinders lying above that for ordinary cylinders. The scales for $[\eta]$ and μ lie to the left and right, respectively.

The empirical Mark—Houwink law relates to the scaling between mass and intrinsic viscosity over a set of molecular weight fractions constituting a homologous series:

$$[\eta]_P = K'M^{\mu} \tag{36}$$

where M is the molecular weight and K' is a constant. Because of subtle effects in the mass-scaling (e.g., the "draining" phenomenon for random coils) the effective exponent μ often has weak molecular mass dependence. Nevertheless, given a sufficiently narrow molecular weight range, empirical intrinsic viscosity data are usually linear on a log—log plot and both K' and μ are regarded as constants for a given polymer—solvent system. The exponent μ is an indicator of the structure of the solute particle: $\mu \approx 0$ indicates globular molecules, $\mu \approx 0.5$ indicates the Θ-state, μ in the range 0.5 to 0.75 indicates departures from the Θ-state due either to solvent quality or chain stiffness, while μ in excess of 0.75 is usually only attributable to chain stiffness.[74] Because of eq 12, the value $\mu \approx 2$ is often cited for rigid rods. However, as we show presently, because of the ln A terms, μ never attains this value for physically realizable rods.

Since for long rods, length and mass are proportional, we can write the Mark—Houwink law in this form:

$$[\eta] = K\left(\frac{L}{d}\right)^{\mu} = KA^{\mu} \tag{37}$$

where the law is regarded as applying to a homologous series of rods: A sequence of rods with d constant and with L variable. Figure 11 displays log—log plots of $[\eta]$ as a function of A generated by the Padé approximants for both cylinders and blunt cylinders. It also shows a plot of the exponent μ as a function of A calculated from eq 17 using the relation

$$\mu = \left[\frac{\partial(\ln[\eta])}{\partial(\ln A)}\right]_d = \frac{A}{[\eta]}\left[\frac{\partial[\eta]}{\partial A}\right]_d \tag{38}$$

Obviously, true power-law behavior is not exhibited by rods over this range of aspect ratios since μ tends to the asymptotic value of 2 only very slowly. Homologous series of rodlike particles can always be expected to enter the semiflexible regime long before ln A gets large enough to permit $\mu \approx 2$. [4] In fact, we are unaware of any empirical systems that have ever displayed values near 2.

We also note the utility of the Mark—Houwink construction in characterizing macromolecular shape. For example, Aharoni[4] has measured intrinsic viscosities for a number of nominally rodlike polymeric aromatic amides, obtaining $\mu \cong 1.2$ at contour length to diameter ratios in the vicinity of 100. According to Figure 11, such values of μ occur only at aspect ratios below 10 for cylinders, which most likely indicates that these polymers are semiflexible or wormlike, rather than rodlike.

5. Effects of Polydispersity

A discussion of polydispersity is relevant because many rodlike systems, e.g., carbon nanotubes, are difficult to fractionate. Obviously, if more than one species is present, then their effect on the virial expansion is additive:

$$\eta = \eta_0(1 + \sum [\eta]_i \phi_i + ...) \tag{39a}$$

$$\eta = \eta_0(1 + \sum [\eta]_{Pi} c_i + ...) \tag{39b}$$

It follows that the intrinsic viscosity of a solution containing a distribution of species is given by

$$[\bar{\eta}] = \frac{\sum_i N_i V_i [\eta]_i}{\sum_i N_i V_i} \quad \text{or} \quad [\bar{\eta}]_P = \frac{\sum_i N_i m_i [\eta]_{Pi}}{\sum_i N_i m_i} \tag{40}$$

where the bar is used to indicate the intrinsic viscosity of a distribution of molecular weights. Here N_i is the number of molecules of species i, V_i and m_i are the volume and mass of each molecule of species i. If we assume that all the species present have the same diameter and density, then the volume and the mass of any species are proportional to the length, and we can index each species by its length. Therefore, we can write

$$[\bar{\eta}] = \frac{\int_0^\infty [\eta] L f(L)\, \mathrm{d}L}{\int_0^\infty L f(L)\, \mathrm{d}L} \quad \text{or} \quad [\bar{\eta}]_P = \frac{\int_0^\infty [\eta]_P L f(L)\, \mathrm{d}L}{\int_0^\infty L f(L)\, \mathrm{d}L} \tag{41}$$

where $f(L)\,\mathrm{d}L$ is the mole fraction of rods with length between L and $L + \mathrm{d}L$.

It is customary to define the viscosity-average molecular weight of a distribution of molecules all belonging to some homologous series as the molecular weight of a monodisperse member of the homologous series that has the same intrinsic viscosity as the distribution. Obviously, for rods, we can extend the definition to viscosity-average length or aspect ratio. It is well-known that if we assume that the Mark–Houwink exponent is $\mu = 1$, we obtain $\bar{A}_v = \bar{A}_w$, i.e., the viscosity-average aspect ratio is equal to the weight-average aspect ratio. The assumption $\mu = 2$ gives $\bar{A}_v = (\bar{A}_z\bar{A}_w)^{1/2}$; i.e., the viscosity-average aspect ratio equals the geometric mean of the z- and the weight-averages. In actuality, because the effective μ is always between 1 and 2, we can expect the following inequality:[75]

$$\bar{A}_w \le \bar{A}_v \le (\bar{A}_w\bar{A}_z)^{1/2} \tag{42}$$

Furthermore, since the effective μ increases toward 2, we can expect the viscosity average to move toward the upper end of the range of eq 42 with increasing aspect ratio. We have investigated this by computing

$$\Delta = \frac{\bar{A}_v - \bar{A}_w}{(\bar{A}_w\bar{A}_z)^{1/2} - \bar{A}_w} \tag{43}$$

for a large number of hypothetical length distributions (including bimodal, square, increasing and decreasing ramp, and exponentially decreasing distributions). Defined in this way, Δ varies between 0 and 1 as $\bar{A}_v$ varies within the range of eq 42. As expected, Δ is correlated with $\bar{A}_n$. The following quadratic expression can be used to approximate the correlation curve:

$$\Delta \approx 0.42 + 0.24(\log_{10} \bar{A}_n) - 0.03(\log_{10} \bar{A}_n)^2 \tag{44}$$

The correlation is displayed in the Supporting Information. Obviously, eqs 43 and 44 can be used to estimate $\bar{A}_v$ from $\bar{A}_n$, $\bar{A}_w$, and $\bar{A}_z$.

6. Conclusions

We have provided accurate expressions for the hydrodynamic radius and the intrinsic viscosity of cylinders over a range of aspect ratios that is of experimental interest in characterizing rodlike particles. These were obtained by applying our numerical path-integration technique and determining Padé approximants that approximate the raw integration data. Our results allow us to judge the accuracy of all previous determinations of these properties. We find that many of the proposed expressions are not too accurate. However, the Batchelor[44] and the Tirado–de la Torre[28,29,32,65] expressions for the hydrodynamic radius are reasonably accurate. Also two formulas from Miles[64] for electrostatic properties give, via the hydrodynamic–electrostatic approximation, accurate predictions for the hydrodynamic radius and the intrinsic viscosity, respectively. The fundamental problem is that expansions about the slender-body limit converge extremely slowly.

We also show that the practice of modeling rodlike objects as effective ellipsoids of revolution is inaccurate. If we try to replace a cylinder with an ellipsoid of the same length and the same aspect ratio, we obtain the curves labeled A3 and A11 in Figures 3–5. If we try to replace a cylinder with an ellipsoid of the same length, but adjust the aspect ratio of the ellipsoid to agree with the transport properties of the cylinder, we find that two different ellipsoids are required, one for the hydrodynamic radius and one for the hydrodynamic volume. Moreover, neither of these ellipsoids reproduces the gyration radius of the cylinder. However, it is always possible to describe a general rodlike particle, which does not taper, by an effective cylinder having the same length, hydrodynamic radius, hydrodynamic volume, and radius of gyration.

We also consider the ratios R_g/R_h, R_η/R_h, and $R_g^3/V[\eta]$. These are of interest because they combine the results of two different experiments into scale-invariant measures of the particle shape. We show that for rods, all three ratios are linear in the logarithm of the aspect ratio.

We also consider the Mark–Houwink scaling exponent μ. A common expectation is that $\mu = 2$ for rods. However, because of the slow convergence to asymptotic behavior, we doubt that any objects will ever be observed with μ as large as 2. Rather, we expect such objects to enter the semiflexible regime, characterized by smaller μ values, long before reaching the asymptotic value of 2.

For this reason, the assertion that the viscosity-average length of rodlike particles is equal to the geometric mean of the weight-average and the z-average, $\bar{A}_v = (\bar{A}_z\bar{A}_w)^{1/2}$, is an oversimplification. This geometric mean proves to be an upper bound to the actual viscosity average.

It must also be appreciated that the rigid-rod model is normally an idealization of particle structure. All such particles have some flexibility, measured by a persistence length, and the rod model is only appropriate when the contour length is much smaller than the persistence length. For many of these particles, the wormlike chain is the more appropriate model. Correspondingly, we have computed the intrinsic viscosity and friction coefficient of wormlike chains which should provide a more reliable model for the characterization of carbon nanotubes and other slender polymeric structures. [60]

Acknowledgment. We are grateful to Sergio Aragon of San Francisco State University for providing the results of boundary element computations for rods.[58] Our computations were performed using the High Performance Computing Facility of the Stevens Institute of Technology.

Literature Expressions for the Hydrodynamic Radius and Intrinsic Viscosity of Cylinders

A number of formulas for the hydrodynamic radius and intrinsic viscosity of cylinders have been given in the literature. They are summarized in this appendix for comparison with our own results.

A. Hydrodynamic Radius. A current textbook gives the following formula for the hydrodynamic radius of cylinders, [76] which has been used to construct the curve labeled A1 in Figure 3:

$$\frac{R_{\mathrm{h}}}{r} = A[\ln(2e^{-0.3}A)]^{-1} \tag{A1}$$

The following expression is obtained from Miles' electrostatic treatment of cylinders, [64] and leads to the curve labeled A2 in Figure 3:

$$\frac{R_{\mathrm{h}}}{r} = A[\ln(4e^{-1}A)]^{-1} \tag{A2}$$

Because $2e^{-0.3} \approx 4e^{-1}$, eqs A1 and A2 are nearly the same. As can be seen in Figure 3, both are accurate to 3% or better at all aspect ratios greater than about 4.

The hydrodynamic radius of the ellipsoid of revolution that has the same total length and the same aspect ratio as a cylinder is given by[76]

$$\frac{R_{\mathrm{h}}}{r} = \frac{(A^2-1)^{1/2}}{\ln[A+(A^2-1)^{1/2}]} \tag{A3}$$

Curve A3 in Figure 3 and 4 results from the above. Equation A3 underestimates the hydrodynamic radius by 7% or more at all aspect ratios, A, below 100.

The following formula has been given by Broersma: [21,22,26,30,31]

$$\frac{R_{\mathrm{h}}}{r} = A\left[\ln(2A) - \frac{1}{2}(\gamma_{\parallel}+\gamma_{\perp})\right]^{-1} \tag{A4}$$

with $\gamma_{\parallel} = 1.27 - 7.4(z - 0.34)^2$, $\gamma_{\perp} = 0.19 - 4.2(z - 0.39)^2$, and $z = [\ln(2A)]^{-1}$, and generates the curve labeled A4 in Figure 3. Errors above 5% are seen at all aspect ratios below 50.

Tirado and co-workers[28,29,32,65] present this formula,

$$\frac{R_{\mathrm{h}}}{r} = \frac{A}{\ln(A)+\nu}, \quad \nu = 0.312 + 0.565A^{-1} - 0.1A^{-2} \tag{A5}$$

which produces the curve labeled A5 in Figure 3. It was only developed for aspect ratios in the range $2 < A < 30$, but our computation indicates that it is accurate to better than 2% at all aspect ratios above 2.

Batchelor[44] gives the following expression for the hydrodynamic radius of cylinders:

$$\frac{R_{\mathrm{h}}}{r} = 2Az(g_1^{-1} + g_2^{-1})^{-1} \tag{A6a}$$

$$g_1(z) = \frac{1+0.307z}{1-0.5z} + 0.426z^2 \tag{A6b}$$

$$g_2(z) = \frac{1+0.307z}{1+0.5z} + 0.118z^2 \tag{A6c}$$

$$z = [\ln(2A)]^{-1} \tag{A6d}$$

Equation A6 is accurate to 2% or better at all aspect ratios above 5, and generates the curve labeled A6 in Figure 3.

B. Intrinsic Viscosity. The following formula has been employed recently in the interpretation of the intrinsic viscosity of carbon nanotubes,[8,9] and generates curve A7 in Figure 5:

$$[\eta] = \frac{8A^2z}{45}f(z) \tag{A7a}$$

$$f(z) = \frac{1+0.64z}{1-1.5z} + 1.659z^2 \tag{A7b}$$

$$z = [\ln(2A)]^{-1} \tag{A7c}$$

The $f(z)$ factor figures in a formula due to Batchelor for the elongational viscosity.[23,48] Therefore, its use for the shear viscosity might be questionable. In any case, eq A7 overestimates the intrinsic viscosity by 12% or more for all aspect ratios below 100.

Yamakawa[25] provides this formula

$$[\eta] = \frac{8A^2}{45}[\ln(4e^{-25/12}A)]^{-1} \tag{A8}$$

which underestimates the intrinsic viscosity by approximately 10% to 20% for all aspect ratios between 3 and 30. It produces the curve A8 in Figure 5.

The Miles' calculation[64] gives (if we use $q_\eta = 0.8$)

$$[\eta] = \frac{8A^2}{45}[\ln(4e^{-7/3}A)]^{-1} \tag{A9}$$

producing curve A9 in Figure 5. It is accurate to 5% or better for all aspect ratios above about 5. Coincidentally, it predicts the intrinsic viscosity of blunt cylinders to 2% or better at all aspect ratios above 10.

Nakajima, Ookubo, Komatsubara, and Wada[27] present the formula

$$[\eta] = \frac{8A^2}{45[\ln(A) - 0.66]} \tag{A10}$$

It is numerically quite close to the Yamakawa formula, eq A8, and generates curve A10 of Figure 5.

Let $[\eta]_{\mathrm{ell}}$ represent the intrinsic viscosity of the ellipsoid that has the same length and aspect ratio as the cylinder in question. If V_{ell} and V_{cyl} are the respective volumes of said ellipsoid and cylinder, then obviously, the following equation results from the attempt to estimate the intrinsic viscosity of the cylinder from that of the ellipsoid:

$$[\eta] = \frac{[\eta]_{\mathrm{ell}}V_{\mathrm{ell}}}{V_{\mathrm{cyl}}} \tag{A11}$$

Curve A11 in Figure 5 is generated by eq A11. We determined $[\eta]_{\mathrm{ell}}$ using an unpublished Padé developed in our laboratory, but exact expressions for $[\eta]_{\mathrm{ell}}$ are also available.[13,16,18]

Supporting Information Available: Text discussing higher-accuracy Padé approximants for the hydrodynamic radius and intrinsic viscosity of cylinders and data on chains of spheres (model B) including tables of data and figures showing the difference between blunt and ordinary cylinders, polarizability/capacity loci for slender bodies, and viscosity-average lengths of cylinders. This material is available free of charge via the Internet at http://pubs.acs.org.

References and Notes

(1) Berry, G. C. *J. Polym. Sci.: Polym. Symp.* **1978**, *65*, 143–172.
(2) Wong, C.-P.; Ohnuma, H.; Berry, G. C. *J. Polym. Sci.: Polym. Symp.* **1978**, *65*, 173–192.
(3) Helminiak, T. E.; Berry, G. C. *J. Polym. Sci.: Polym. Symp.* **1978**, *65*, 107–123.
(4) Aharoni, S. M. *Macromolecules* **1987**, *20*, 2010–2017.
(5) Wierenga, A. M.; Philipse, A. P. *J. Colloid Interface Sci.* **1996**, *180*, 360–370.
(6) van Bruggen, M. P. B.; Lekkerkerker, H. N. W.; Dhont, J. K. G. *Phys. Rev. E* **1997**, *56*, 4394–4403.

(7) Shaffer, M. S. P.; Windle, A. H. *Macromolecules* **1999**, *32*, 6864–6866.

(8) Davis, V. A.; Ericson, L. M.; Parra-Vasquez, A. N. G.; Fan, H.; Wang, Y.; Prieto, V.; Longoria, J. A.; Ramesh, S.; Saini, R. K.; Kittrell, C.; Billups, W. E.; Adams, W. W.; Hauge, R. H.; Smalley, R. E.; Pasquali, M. *Macromolecules* **2004**, *37*, 154–160.

(9) Parra-Vasquez, A. N. G.; Stepanek, I.; Davis, V. A.; Moore, V. C.; Haroz, E. H.; Shaver, J.; Hauge, R. H.; Smalley, R. E.; Pasquali, M. *Macromolecules* **2007**, *40*, 4043–4047.

(10) Bauer, B. J.; Becker, M. L.; Bajpai, V.; Fagan, J. A.; Hobbie, E. K.; Migler, K.; Guttman, C. M.; Blair, W. R. *J. Phys. Chem. C* **2007**, *111*, 17914–17918.

(11) Fagan, J. A.; Becker, M. L.; Chun, J.; Hobbie, E. K. *Adv. Mater.* **2008**, *20*, 1609−1613.

(12) Fagan, J. A.; Becker, M. L.; Chun, J.; Nie, P.; Bauer, B. J.; Simpson, J. R.; Hight-Walker, A.; Hobbie, E. K. Centrifugal Length Separation of Carbon Nanotubes. *Langmuir* Submitted for publication.

(13) Jeffery, G. B. *Proc. R. Soc. London, Ser. A* **1922**, *102*, 161–179.

(14) Onsager, L. *Phys. Rev.* **1932**, *40*, 1028.

(15) Perrin, F. *J. Phys. Radium* **1936**, *7*, 1–11.

(16) Simha, R. *J. Phys. Chem.* **1940**, *44*, 25–34.

(17) Simha, R. *J. Chem. Phys.* **1945**, *13*, 188–195.

(18) Saito, N. *J. Phys. Soc. Jpn.* **1951**, *5*, 297–301.

(19) Haltner, A. J.; Zimm, B. H. *Nature* **1959**, *184*, 265–266.

(20) Gluckman, M. J.; Pfeffer, R.; Weinbaum, S. *J. Fluid Mech.* **1971**, *50*, 705–740.

(21) Broersma, S. *J. Chem. Phys.* **1960**, *32*, 1626–1631.

(22) Broersma, S. *J. Chem. Phys.* **1960**, *32*, 1632–1635.

(23) Batchelor, G. K. *J. Fluid Mech.* **1971**, *46*, 813–829.

(24) Yamakawa, H.; Yamaki, J. *J. Chem. Phys.* **1973**, *58*, 2049–2055.

(25) Yamakawa, H. *Macromolecules* **1975**, *8*, 339–342.

(26) Newman, J.; Swinney, H. L.; Day, L. A. *J. Mol. Biol.* **1977**, *116*, 593–606.

(27) Nakajima, H.; Ookubo, N.; Komatsubara, M.; Wada, Y. *Polym. Prepr., Am. Chem. Soc.* **1979**, *20*, 49–52, The formula as cited in this reference differs by a factor of 4 from what we have written in eq A10. Assuming this to be inadvertent, we have converted the front factor so that eq A10 has the correct asymptotic behavior.

(28) Tirado, M. M.; Garcia de la Torre, J. *J. Chem. Phys.* **1979**, *71*, 2581–2587.

(29) Tirado, M. M.; Garcia de la Torre, J. *J. Chem. Phys.* **1980**, *73*, 1986–1993.

(30) Broersma, S. *J. Chem. Phys.* **1981**, *74*, 6989–6990.

(31) Zero, K. M.; Pecora, R. *Macromolecules* **1982**, *15*, 87–93.

(32) Tirado, M. M.; Martinez, C. L.; Garcia de la Torre, J. *J. Chem. Phys.* **1984**, *81*, 2047–2052.

(33) Ui, T. J.; Hussey, R. G.; Roger, R. P. *Phys. Fluids* **1984**, *27*, 787–795.

(34) Tracy, M. A.; Pecora, R. *Annu. Rev. Phys. Chem.* **1992**, *43*, 525–557.

(35) Clarke, N. S. *J. Fluid Mech.* **1972**, *52*, 781–793.

(36) Johnson, R. E. *J. Fluid Mech.* **1980**, *99*, 411–431.

(37) Johnson, R. E.; Wu, T. Y. *J. Fluid Mech.* **1979**, *95*, 263–277.

(38) Goren, S. L.; O'Neill, M. E. *J. Fluid Mech.* **1980**, *101*, 97–110.

(39) Haber, S.; Brenner, H. *J. Colloid Interface Sci.* **1994**, *97*, 496–514.

(40) Zwanzig, R., *J. Chem. Phys.* **1966**, *45*, 1858–1859.

(41) Cox, R. G. *J. Fluid Mech.* **1970**, *44*, 791–810.

(42) Tillett, J. P. K. *J. Fluid Mech.* **1970**, *44*, 401–417.

(43) Batchelor, G. K. *J. Fluid Mech.* **1970**, *41*, 545–570.

(44) Batchelor, G. K. *J. Fluid Mech.* **1970**, *44*, 419–440.

(45) Yamakawa, H. *Modern Theory of Polymer Solutions*; Harper & Row: New York, 1971.

(46) Brenner, H. *Int. J. Multiphase Flow* **1974**, *1*, 195–341.

(47) Doi, M.; Edwards, S. F. *The Theory of Polymer Dynamics*; Oxford University Press: Oxford, U.K., 1986.

(48) Powell, R. L. *J. Stat. Phys.* **1991**, *62*, 1073–1094.

(49) Petrie, C. J. S. *J. Non-Newtonian Fluid Mech.* **1999**, *87*, 369–402.

(50) Hubbard, J. B.; Douglas, J. F. *Phys. Rev. E* **1993**, *47*, 2983–2986.

(51) Douglas, J. F.; Zhou, H.-X.; Hubbard, J. B. *Phys. Rev. E* **1994**, *49*, 5319–5331.

(52) Douglas, J. F.; Garboczi, E. J. *Adv. Chem. Phys.* **1995**, *91*, 85–153.

(53) Given, J. A.; Hubbard, J. B.; Douglas, J. F. *J. Chem. Phys.* **1997**, *106*, 3761–3771.

(54) Zhou, H.-X.; Szabo, A.; Douglas, J. F.; Hubbard, J. B. *J. Chem. Phys.* **1994**, *100*, 3821–3826.

(55) Mansfield, M. L.; Douglas, J. F.; Garboczi, E. J. *Phys. Rev. E* **2001**, *64*, 061401.

(56) Mansfield, M. L.; Douglas, J. F. *Condens. Matter Phys.* **2002**, *5*, 249–274.

(57) Kang, E.-H.; Mansfield, M. L.; Douglas, J. F. *Phys. Rev. E* **2004**, *69*, 031918.

(58) Aragon, S. Private communication.

(59) One source of the inaccuracy of slender-body theory has been shown to be due to the description of polymer chains as hydrodynamic point sources or hydrodynamic "beads." Good convergence normally requires a relatively large number of beads. A precise examination of this approximation for tori is given by Goren and O'Neill,[38] where comparison is made with exact computations of the translational and rotational friction coefficients so there is no uncertainty in the comparison. See also: Mansfield, M. L.; Douglas, J. F.; Irfan, S.; Kang, E.-H. *Macromolecules* **2007**, *40*, 2575–2589.

(60) Mansfield, M. L.; Douglas, J. F. Transport Properties of Wormlike Chains with Applications to Double Helical DNA and Carbon Nanotubes. Submitted to *Macromolecules*.

(61) Mansfield, M. L.; Douglas, J. F. Manuscript in preparation.

(62) Mansfield, M. L. Douglas, J. F. Submitted to *Phys. Rev. E*.

(63) The equivalence of hydrodynamic volume, rather than intrinsic viscosity, is also seen in eqs 12 and 14. If these are each multiplied by the respective volumes, we see that the ellipsoid and the cylinder tend to the same asymptotic expression for the hydrodynamic volume.

(64) Miles, J. W. *J. Appl. Phys.* **1967**, *38*, 192–196.

(65) Eimer, W.; Pecora, R. *J. Chem. Phys.* **1991**, *94*, 2324–2329.

(66) It is, however, true that oblate (disklike) cylinders can be replaced by equivalent oblate ellipsoids of revolution. In this limit, convergence is controlled by the aspect ratio itself and not its logarithm.

(67) Garcia de la Torre, J.; Carrasco, B. *Prog. Colloid Polym. Sci.* **1999**, *113*, 81–86.

(68) Fortran code or an Excel spreadsheet are also available upon request.

(69) Boedtker, H.; Simmons, N. S. *J. Am. Chem. Soc.* **1958**, *80*, 2550–2556.

(70) Schachman, H. K.; Kauzmann, W. J. *J. Phys. Chem.* **1949**, *53*, 150–162.

(71) We are uncertain why two independent results for the intrinsic viscosity of the tobacco mosaic virus show such a large discrepancy. However, problems either with fractionation or dispersion in solution come to mind.

(72) Jeans, J. H. *The Mathematical Theory of Electricity and Magnetism*, 5th ed.; Cambridge University Press: London, 1941.

(73) Defined as they are by transport properties, it would be appropriate to call either R_h or R_η a "hydrodynamic" radius, and both have been so called in the literature. But there is no reason to expect them to be equal except for spheres. Nevertheless, there is a great deal of empirical and computational evidence that $R_\eta/R_h \cong 1$ for all bodies *except* highly prolate rods, ellipsoids, etc. Therefore this ratio is a good slender-body indicator. A complete study will be published later. [Kang, E.-H.; Mansfield, M. L.; Douglas, J. F. Manuscript in preparation.] See also ref 67.

(74) Flory, P. J. *Statistical Mechanics of Chain Molecules*; Wiley: New York, 1969.

(75) Because the Mark−Houwink law is not followed rigorously, the inequality of eq 42 is sometimes violated. Nevertheless, from data reported in the Supporting Information, it is obvious that over most of the range of aspect ratios, eq 42 is obeyed.

(76) VanHolde, K. E.; Johnson, W. C.; Ho, P. S. *Principles of Physical Biochemistry*, 2nd ed.; Pearson Prentice Hall: Upper Saddle River, NJ, 2006.

MA702839W